Cement and Concrete Research 135 (2020) 106107

Contents lists available at ScienceDirect

Cement and Concrete Research

journal homepage: www.elsevier.com/locate/cemconres

Mechanisms of autogenous shrinkage of alkali-activated slag and fly ash pastes

Zhenming Li[a,*], Tianshi Lu[a], Xuhui Liang[a], Hua Dong[a], Guang Ye[a,b]

[a] Department of Materials, Mechanics, Management & Design, Faculty of Civil Engineering and Geoscience, Delft University of Technology, Delft, the Netherlands
[b] Magnel Laboratory for Concrete Research, Department of Structural Engineering, Ghent University, Ghent, Belgium

ARTICLE INFO

Keywords:
Shrinkage
Mechanism
Alkali-activated slag
Fly ash
Modelling

ABSTRACT

This study aims to provide a better understanding of the autogenous shrinkage of slag and fly ash-based alkali-activated materials (AAMs) cured at ambient temperature. The main reaction products in AAMs pastes are C-A-S-H type gel and the reaction rate decreases when slag is partially replaced by fly ash. Due to the chemical shrinkage and the fine pore structure of AAMs pastes, drastic drop of internal relative humidity is observed and large pore pressure is generated. The pore pressure induces not only elastic deformation but also a large creep of the paste. Besides the pore pressure, other driving forces, like the reduction of steric-hydration force due to the consumption of ions, also cause a certain amount of shrinkage, especially in the acceleration period. Based on the mechanisms revealed, a computational model is proposed to estimate the autogenous shrinkage of AAMs. The calculated autogenous shrinkage matches well with the measured results.

1. Introduction

Alkali-activated materials (AAMs) have emerged as eco-friendly alternatives to ordinary Portland cement (OPC) based binders [1]. Compared to cement production, the production of AAMs entails around 25–50% lower CO_2 emissions and > 40% lower embodied energy [2,3]. However, a wide utilization of AAMs in infrastructures has not been realized yet due to the insufficient knowledge of the performances of AAMs. Blast-furnace slag (hereinafter termed slag as an abbreviation) and coal fly ash, as industrial by-products, are the most widely used raw materials for synthesizing AAMs [1,4]. While it has been known that alkali-activated slag and fly ash systems can show high strength, good chemical resistance and fire resistance [5–7], the autogenous shrinkage of these materials has not been well understood.

Previous studies have shown that slag and fly ash based AAMs can show high autogenous shrinkage [8–13]. However, regarding the mechanisms behind the high autogenous shrinkage, no consensus has been reached.

Collins and Sanjayan [14] attributed the high autogenous shrinkage of alkali-activated slag (AAS) to the dense pore structure of the paste. Their experimental results showed that up to 80% of the pores in AAS paste activated by Na_2SiO_3 were mesopores (1.25–25 nm), while OPC paste contained only 36.4% of mesopores and a larger percentage of macropores (25–5000 nm). Given the fine pore structure of AAS, a certain chemical shrinkage would result in a small radius of menisci in the paste [15], which means a high pore pressure. The large fraction of mesopore volume in AAS was further confirmed by Lee et al. [16]. Besides the radius of the menisci, surface tension in AAS was also reported to be higher than that in OPC according to Ballekere Kumarappa et al. [17]. The large quantity of ions induced a high surface tension of the pore solution in AAS and consequently resulted in large pore pressure. Cartwright et al. [18] reported that AAS had a higher saturation degree and lower elastic modulus than OPC, thus showed a higher autogenous shrinkage. Ye and Radlińska [19] proposed another reason of the large shrinkage of AAS from the gel structure point of view. Due to the incorporation of alkali cations, the aluminium-modified calcium silicate hydrate (C-A-S-H) gel was found to collapse and redistribute more easily than the calcium silicate hydrate (C-S-H) gel under pore pressure, therefore C-A-S-H gel shows a pronounced visco-elastic/visco-plastic behaviour at the macroscopic scale.

While the above-mentioned studies provided different insights into shrinkage mechanism of AAS, their common assumption is that the driving force of the autogenous shrinkage of AAS is pore pressure like the assumption for OPC. However, different opinions were held by other researchers. For example, Ma and Dehn [20] stated that self-desiccation seems not to be the exclusive reason why autogenous shrinkage of the AAS concrete is doubled compared to the high-strength OPC concrete. Uppalapati and Cizer [21] reported that the autogenous

* Corresponding author.
E-mail address: z.li-2@tudelft.nl (Z. Li).

https://doi.org/10.1016/j.cemconres.2020.106107
Received 5 February 2020; Received in revised form 3 May 2020; Accepted 10 May 2020
Available online 22 May 2020

shrinkage of AAS is also related to the contraction induced by silica polymerization reaction during the formation of C-A-S-H gels.

Regarding the alkali-activated slag-fly ash (AASF) paste, Fang et al. [22] reported that the volume contraction caused by chemical shrinkage in fresh state occupied approximately 70% of the total autogenous shrinkage in the first 24 h. However, this finding seems contrary to the results of Lee et al. [16], who claimed that the autogenous shrinkage of AASF mortar occurs mainly due to self-desiccation in the hardened state rather than the volume contraction converted from the chemical shrinkage in the fresh state. Aydin [23] reported that the lower autogenous shrinkage of AASF than that of AAS is because the shrinkage of C-A-S-H gel is restrained by the 3D structured sodium aluminosilicate hydrate (N-A-S-H) gels produced by the activation of fly ash.

In summary, no convincing hypothesis has been proposed yet to completely explain the autogenous shrinkage of AAMs made from slag and fly ash, let alone predict the autogenous shrinkage of AAMs by models [22,24]. A better understanding of the shrinkage mechanisms is a required for the prediction of the cracking potential of AAMs under the restrained condition and the development of shrinkage-mitigating strategies.

This study aims at investigating the mechanism of the autogenous shrinkage of AAMs made of slag and fly ash. The autogenous shrinkage of AAS and AASF pastes is measured and compared with that of OPC paste. Second, various techniques are applied to characterize the microstructure formation of AAS and AASF pastes, with regard to the reaction products, reaction rate and pore structures. The parameters that influence the autogenous shrinkage of AAMs, e.g., chemical shrinkage, internal relative humidity (RH) and elastic modulus evolution of the pastes, are compressively investigated. The driving forces of the autogenous shrinkage of AAMs and the deformability of the pastes are then clarified. Based on the experimental results, the autogenous shrinkage of AAMs is modelled considering both elastic and non-elastic/creep deformations.

2. Materials and experiments

2.1. Raw materials and mixture proportions

The main raw materials used were slag supplied by Ecocem Benelux BV and fly ash from Vliegasunie BV. The chemical compositions of slag and fly ash (FA1) were determined by X-ray fluorescence (XRF) (as shown in Table 1). The fly ash complies with Class F (EN 450, ASTM C618) since it has low CaO content (< 10% reactive CaO) and a content of "SiO_2 + Al_2O_3 + Fe_2O_3" higher than 70%. The particle size of slag ranges from 0.1 to 50 μm, with a d_{50} of 18.3 μm. The particle size of FA1 is between 0.14 and 138 μm, with a d_{50} of 48.1 μm. In Section 3.2.3, two other fly ashes (FA2 and FA3) produced by the same supplier but in different batches will be used to reveal the influence of the variation in fly ash. The chemical compositions of FA2 and FA3 are also shown in Table 1. It can be seen that the chemical compositions of three batches of fly ash are slightly different. In Section 3.1, OPC paste made of CEMI 52.5 R is used as a reference mixture. The chemical composition of CEMI 52.5 R is also shown in Table 1.

Table 2
Mixture compositions of the pastes.

Mixture	Slag (g)	Fly ash (g)	Cement (g)	SiO_2 (mol)	Na_2O (mol)	H_2O (g)
AAS	1000	–	–	1.146	0.76	384
AASF	500	500	–	1.146	0.76	384
Cement paste	–	–	1000	–	–	400

Alkali-activated slag paste and alkali-activated slag-fly ash blended paste are studied. For the slag and fly ash blended systems, one slag to fly ash weight ratio, 50–50%, is focused in this research. Other ratios like 30–70% and 70–30% do not have substantial differences on the microstructure and shrinkage behaviors of the paste [25–27], so these ratios are not concerned in this research. Alkali-activated fly ash paste does not show considerable stiffness and strength at ambient condition, and is therefore not studied in this paper. The mix design of the pastes is shown in Table 2. The liquid/binder (l/b) ratio of the alkali-activated paste is 0.5, while the water/solid (w/s) ratio of the paste is 0.344 if the SiO_2 and Na_2O in the activator are considered as parts of solid. The water/cement ratio of the cement paste is 0.4.

The alkaline activator was prepared by mixing anhydrous pellets of sodium hydroxide with deionized water and commercial sodium silicate solution. The solution was allowed to cool down for 24 h to room temperature before mixing with the precursors. A Hobart mixer was used for mixing. After premixing of the raw materials for 1 min, activator was added at low speed mixing. The mixing continued at low speed for 1 min and for another 2 min at high speed. All the samples were cured in sealed condition at 20 °C.

2.2. Experimental methods

2.2.1. Setting time

The times of initial and final setting were measured by an automatic Vicat setup with a measurement interval of 5 min [28].

2.2.2. Autogenous shrinkage

Corrugated tubes with a length of 425 mm and a diameter of 28.5 mm were utilized to measure the linear autogenous shrinkage of AAS pastes according to ASTM C1968 [29]. Three replicates were measured for each mixture. The length changes were automatically measured by linear variable differential transformers (LVDTs) until 7 days. After that, the evolution of the autogenous shrinkage becomes slow so the test is stopped. The automatic measurements show a low scatter for triplicate samples, with the relative standard error in the range of 1–2%.

2.2.3. Shrinkage under saturated condition

To investigate the role of self-desiccation in autogenous shrinkage of AAMs, the deformation of the pastes under saturated condition was

Table 1
Chemical compositions of slag, fly ash and cement.

Raw materials	Oxide (wt%)									
	CaO	Al_2O_3	SiO_2	MgO	Fe_2O_3	SO_3	K_2O	TiO_2	Other	L.o.I.
Slag	40.50	13.25	31.77	9.27	0.52	1.49	0.34	0.97	0.21	1.31
FA1	4.8	23.8	56.8	1.5	7.2	0.3	1.6	1.2	1.6	1.2
FA2	5.08	25.74	54.4	1.26	7.88	0.76	1.45	1.22	0.89	1.32
FA3	5.39	26.02	51.92	1.45	9.40	0.84	1.53	1.17	0.98	1.3
OPC	66.72	4.49	16.91	2.41	2.67	2.37	0.63	0.34	0.56	2.9

L.o.I. = Loss on ignition.

measured by a modified corrugated tube method [30,31]. Puertas et at. [32] and Feng et al. [33] measured the deformation of the samples under a RH close to 100%. However, in their methods, the deformation of the paste/mortar can only be measured after the demoulding at 24 h. In this study, the paste was cast into a corrugated tube but only to fill 80% volume of the tube. After that, the top end plug was mounted and the tube was vibrated horizontally. The upper part (25% volume) of the tube was occupied by air. The length change of the tube was then measured following the same procedure as the autogenous shrinkage measurement and the liquid level of the glycol surrounding the tubes was kept slightly lower than the top of the tubes. After final setting of the mixture, three tiny holes were pricked on top of the tube by a needle along the length direction. Drops of activator were then gently added into the tubes through these holes by a syringe until the upper surface of the sample was submerged in liquid (as shown in Fig. 1). Special attention was paid when adding the liquid such that the measurement was not disturbed. According to Tian and Jensen [30], filling only 80% of the tube does not influence the deformation results after final setting of the paste, in relative to the case that the tube is fully filled up. With the method proposed in this study, the deformation can be measured without changing the geometry of the specimen or delaying the starting time of the experiment. An error involved in this method is that the actual reaction degree of the samples could be a bit different from that of the samples under sealed condition, due to externally supplied activator. However, this error is evitable as long as there is exchange of substances between the sample and the environment (e.g. supply of moisture to the sample to keep a high enough RH).

2.2.4. Characterization of the microstructure

X-ray diffraction (XRD) measurement was conducted to examine the crystalline phases in the pastes using a Philips PW 1830 powder X-ray diffractometer with Cu Kα (1.5406 Å) radiation, tube setting of 40 kV and 40 mA, a step size of 0.030° and a 2θ range of 5–70°.

Fourier transform infrared spectroscopy (FTIR) measurement was performed with a TM 100 Optical ATR-FTIR spectrometer over the wavelength range of 600 to 4000 cm^{-1} with a resolution of 4 cm^{-1}.

The reaction heat of AAMs pastes was tracked by a TAM Air isothermal calorimeter (Thermometric). Before measurements, the calorimeter was calibrated at 20 °C for 1 week. Approximately 5 g of paste were cast into each glass vial and were immediately loaded into the measuring channels. The internal diameter of the glass vial was 24.5 mm. The mixing and loading procedures lasted about 15 min from the moment of adding activator. The temperature inside the measured cells was controlled at 20 ± 0.2 °C. The data was recorded every 1 min until 7 days. The reaction heat results were normalized by the weight of the paste.

Nitrogen adsorption test was performed to measure the pore structure (from 0.3 to 300 nm) of the pastes by using Gemini VII 2390 V1.03 (Micromeritics, Brussels, Belgium). The relative pressure ranges from 0.05 to 0.99. The interpretation of the isotherms is based on Barrett-Joyner-Halenda models (BJH) [34].

2.2.5. Chemical shrinkage and internal RH

Dilatometry was used to measure the chemical shrinkage of the pastes as suggested by ASTM C 1608 [35], only the water was replaced by activator to be added onto the surface of the paste [36].

The internal RH of the pastes was measured by Rotronic hygroscopic DT station equipped with HC2-AW measuring cells [37]. Two replicates were tested for each mixture. The nominal error of the sensor was within 2% RH. The sensors were calibrated before and after each measurement using four saturated salt solutions (NaCl, KCl, KNO_3 and K_2SO_4) with equilibrium RH in the range 75–98%. At the curing age of 1 day, 3 days and 7 days, the paste was crashed into small pieces around 0.5 cm^3 and immediately inserted into the hermetic measuring chambers. To consider the influence of dissolved ions on the internal RH, the pore solution was extracted from the paste by a steel die under high pressure and the RH of the pore solution was measured.

2.2.6. Elastic modulus measurement

Elastic modulus is an important parameter to calculate the self-desiccation shrinkage of the paste. Moreover, the evolution of elastic modulus helps to understand the time-zero of the autogenous shrinkage of AAMs, from when tensile stress can be potentially induced in the restrained material. In this study, the elastic modulus was measured automatically using Elasticity Modulus Monitoring through Ambient Response Method (EMM-ARM [38]) from casting until 7 days. The detailed measuring procedure was shown in [38]. Three replicates were tested for each mixture.

3. Results and discussion

3.1. Autogenous shrinkage

The setting time of the pastes determined by Vicat needle is shown in Table 3. The autogenous shrinkage plots starting at the final setting time of the paste.

Fig. 2 shows that the autogenous shrinkage of AAS paste develops rapidly, reaching 3560 μm/m at 1 day and around 6600 μm/m at 7 days. The autogenous shrinkage of AASF is around 40% lower than that of AAS, reaching 1700 μm/m at 1 day and around 3700 at 7 days, but is still much (around 6 times) larger than that of the OPC paste. These findings are in line with the data reported in literature [17,18,20,39,40].

3.2. Microstructure characterization

3.2.1. XRD analysis

The XRD results are shown in Fig. 3. The X-ray diffractogram of slag and fly ash presents a hump around 30.5° and 24° (marked by the dashed lines), respectively, indicating the presence of amorphous phase. While the slag is basically amorphous, several crystalline phases are detected in fly ash, such mullite ($(Al_2O_3)_{1.136}(SiO_2)_{0.728}$), quartz ($SiO_2$) and hematite ($Fe_2O_3$). The peaks at 29° and 49.8° observed in the diffractograms for AAS paste represent the formation of C-A-S-H type gels [41]. The intensity of these peaks decreases when half of the slag is replaced by fly ash. No new crystals are formed in the two pastes, which is in line with the continuous shrinkage of them. In OPC based paste, an expansion can be shown due to the formation of expansive crystals (e.g. ettringite) [42].

With increasing curing age, the main band (29°) for C-A-S-H gel in AAS becomes more intensive. Meanwhile, the peaks for crystals, e.g. the one at 26.5°, become relatively weaker. This indicates that more amorphous reaction products are formed. The spectra for AASF pastes show lower intensity at the humps representing C-A-S-H gel than those for AAS pastes at both 1 day and 7 days. This indicates that the amount of C-A-S-H gel formed in the first week is lower when slag is substituted by fly ash.

3.2.2. FTIR analysis

The FTIR spectra for AAS and AASF pastes all show main bands at near 950 cm^{-1} (Fig. 4), which is assigned to the vibration of Si—O bonds [43]. More specifically, it is associated with the asymmetrical stretching vibrations of Si—O—T (T=Si or Al) bonds and/or Si—O—M bonds (M being alkali metal element) generated by Q^2 units[1], which is the representative structure of aluminosilicate chains containing C-A-S-H type gel [44,45]. The shoulder in the range of 1040–1070 cm^{-1} is also assigned to the asymmetrical stretching of Si—O—T (T=Si or Al) bonds and/or Si—O—M bonds, with a lower extent of Al substitution [46]. The bands located at around 900 cm^{-1} and 660 cm^{-1} are assigned as the deformational vibrations of Si—O—Al or Si—O—Si [44,47].

[1] Q^n denotes the connectivity of the silicate units based on the chemical shift, where n represents the number of Si—O linkages of the unit.

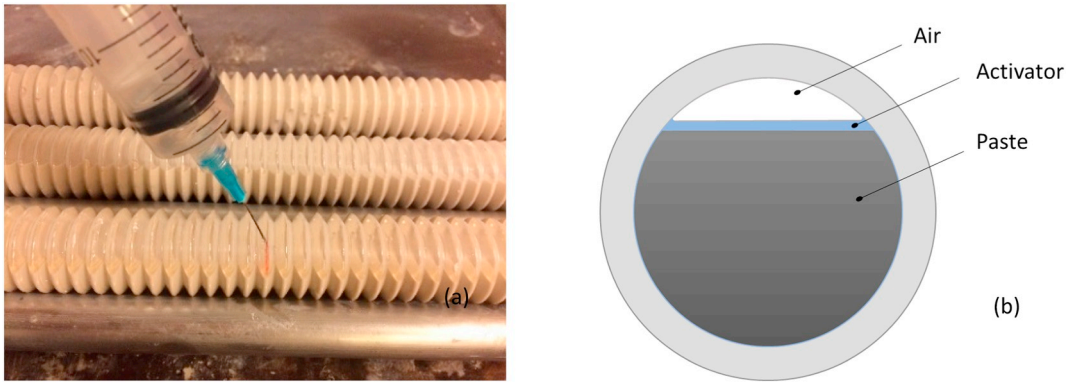

Fig. 1. Using a syringe to add alkali solution into the corrugated tubes (a) which are 80% filled by the paste (b).

Table 3
Vicat setting time of the pastes (min).

Mixture	AAS	AASF	OPC0.4
Initial setting	25	63	240
Final setting	35	103	340

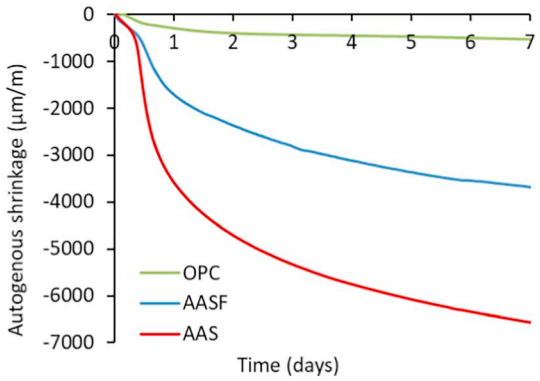

Fig. 2. Autogenous shrinkage of AAS and AASF pastes (l/b = 0.5, w/s = 0.344) in comparison with OPC paste (w/c = 0.4).

The small band at 815 cm^{-1} represents the symmetric stretching vibrations of Si—O (Q^1) [47]. The band at 855 cm^{-1} originates from slag, and the intensity of this band becomes smaller in the spectra for AAS and AASF pastes due to the dissolution of slag and/or the substitution of slag by FA.

In Fig. 4, the signals at 950 cm^{-1}, 900 cm^{-1}, 815 cm^{-1} and 660 cm^{-1} are visible in all spectra for the pastes, but their intensities decrease when fly ash is present. Besides, the spectra for AASF paste show higher intensity in the range of 1000–1200 cm^{-1} than that for AAS paste, due to the presence of unreacted fly ash particles (see the spectrum for FA). These findings indicate that the main reaction products in AAS and AASF are C-A-S-H type gel. The amount of this gel decreases when slag is substituted by fly ash, which confirmed the observations from XRD analysis. No signal representative for N-A-S-H type gel is detected in the spectra. These findings agree with the results obtained by Nedeljković [25] using energy-dispersive X-ray spectroscopy and thermogravimetric analysis.

The first reason why the typical reaction products in heat-cured fly ash-based geopolymer, N-A-S-H gel and zeolites, are not formed in AASF system lies in the low reactivity of fly ash at ambient temperature. The second reason is the instability of N-A-S-H gel in the presence of Ca^{2+} at high alkalinity [44]. Even though the dissolution of fly ash can release a small amount of Si and Al, they tend to involve into the formation of C-A-S-H gel rather than N-A-S-H gel since a large amount of Ca is present in the system due to the dissolution of slag [44,48]. The similar reaction products formed in AAS and AASF pastes determine that the two systems should follow similar mechanisms of autogenous shrinkage.

Comparing the spectra for AASF in Fig. 4(a) and (b), it can be seen that the bands at 950 cm^{-1}, 1050 cm^{-1}, 900 cm^{-1} and 815 cm^{-1} become more intensive at 7 days, which indicates more C-A-S-H gel is formed with the increase of curing age. The intensities of the band at 855 cm^{-1} and the region from 1000 to 1200 cm^{-1} in the spectra for AASF decrease, which indicates that part of the fly ash starts to dissolve

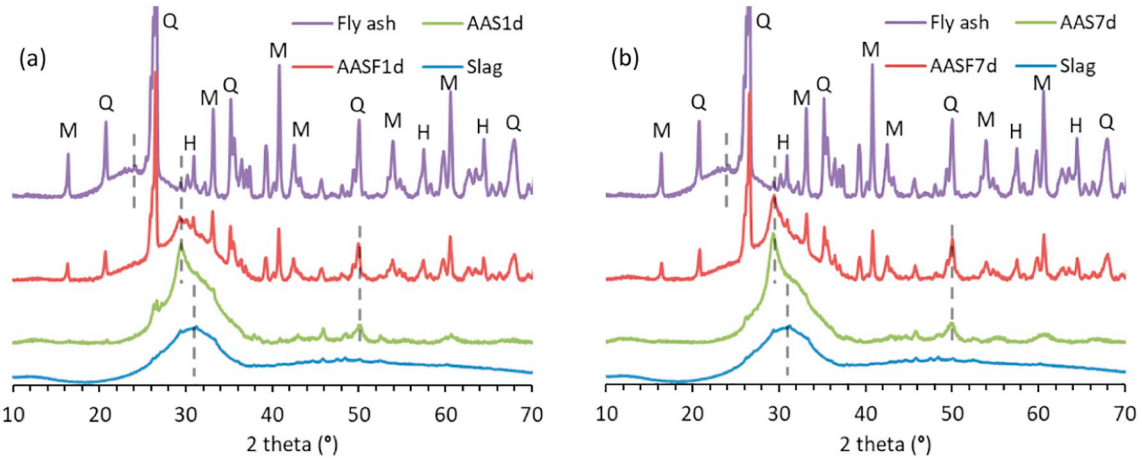

Fig. 3. XRD patterns of AAS and AASF pastes cured for 1 day (a) and 7 days (b), in comparison with precursors (slag and fly ash). M, Q and H stand for mullite, quartz and hematite, respectively.

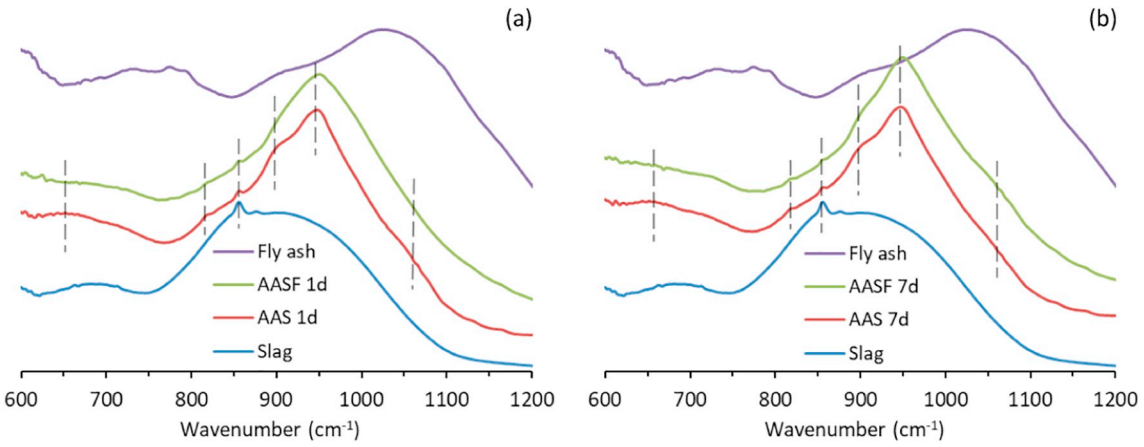

Fig. 4. FITR spectra of AAS and AASF pastes cured for 1 day (a) and 7 days (b), in comparison with precursors (slag and fly ash).

during the 7 days. These changes are less apparent in the spectra for AAS, indicating a small change of the molecular structures of the phases in AAS paste from 1 day to 7 days. The reason can be the high reactivity of slag in alkali environment which does not need 7 days to produce characteristic products [49]. The higher reaction degree of AAS paste compared to AASF paste at 1 day will be further confirmed by the results in next section.

3.2.3. Isothermal heat release

Isothermal calorimetry tests are conducted to investigate the reaction kinetics of AAS and AASF, as shown in Fig. 5. For reason of clarity, the heat flow curves are plotted up to 40 h, while the cumulative heat in the whole measuring period of 168 h is presented. It can be seen from Fig. 5(a) that both pastes experience a dormant period after the initial peak caused by wetting of the raw materials and initial reactions (mainly dissolution). After that, both curves show one main peak, indicating the acceleration period of the reaction. The main heat flow peak indicates the rapid formation of the major products, i.e. C-A-S-H gel, from the reaction of the ions in the activator and new ions dissolved from the precursor. The decrease of the reaction rate after the main peak is normally attributed to the inhibited dissolution of the precursors due to the continuous formation of reaction products surrounding the unreacted particles and the gradually blocked pore space [50].

Compared with AAS, AASF shows a later acceleration period and a lower main heat release peak. Accordingly, the cumulative heat released by AASF is lower than that released by AAS. Given the similar reaction products (C-A-S-H type gels) in the two systems, the lower total heat release of AASFF paste indicates a lower overall reaction degree of the paste.

The main reason for the lower overall reaction degree of AASF paste lies in the low reactivity of fly ash at ambient temperature [51]. It has been well known that the fly ash particles are relatively hard to dissolve no matter in cementitious systems or in alkali-activated systems, despite the existence of amorphous phases in fly ash [51,52]. A longer time or a higher temperature is normally required for fly ash to release a substantial amount of ions in alkali environment [53].

To better understand the role of fly ash in AASF paste, the heat flow curve of AASF paste is compared with the one of alkali-activated slag with quartz (AASQ), where the fly ash in AASF is totally replaced by quartz with different particle sizes. To indicate the repeatability of the calorimetry measurement, three replicates were measured for paste AASF1. Two other fly ashes (FA2 and FA3) ordered from the same supplier but in different batches were also tested, in order to investigate the influence of deviation in the raw materials.

As shown in Fig. 6(a), the heat flow curves for the three replicates of AASF paste show a very small discrepancy, indicating good repeatability of the measurement. Using fly ashes from different batches can induce changes in the peak intensity and the dormant period. Compared to AASF1 paste, AASQ pastes show similar heat flow trends, only the dormant periods are shorter and the main reaction peaks appear earlier. This reason why the acceleration period of AASF paste appears later lies in the Si and Al released from fly ash during dissolution. It has been widely reported in literature that increasing amounts of Si and Al in AAS system, either from the addition of fly ash or from higher modulus (SiO_2/Na_2O) of the activator, would decrease the rate of the formation of C-A-S-H gels [49,50,54–57]. However, it should be noted that the differences in heat flow between AASF and AASQ pastes are much smaller than those between the AASF and AAS, and even smaller than

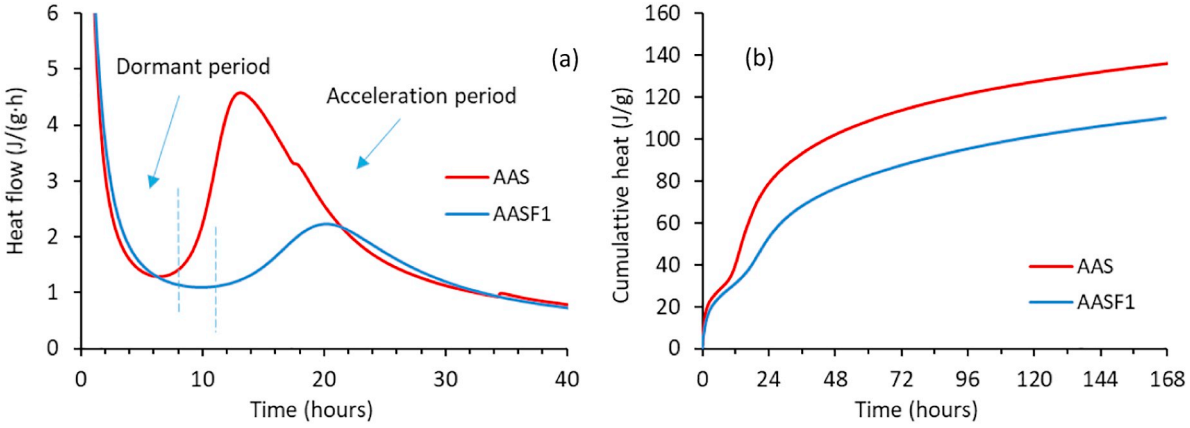

Fig. 5. (a) Heat flow and (b) cumulative heat of AAS and AASF pastes (AASF1 stands for the AASF paste made from FA1).

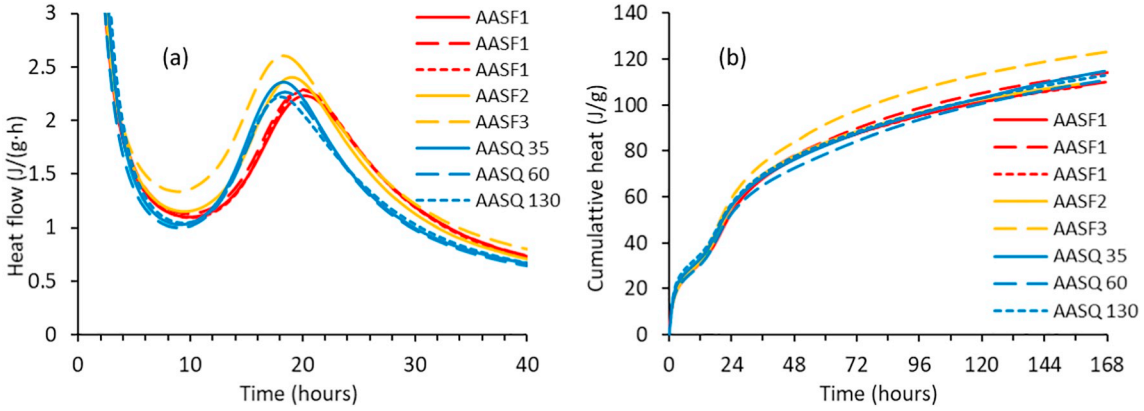

Fig. 6. (a) Heat flow and (b) cumulative heat of AASF pastes made from fly ashes ordered in different batches and AASQ pastes where fly ash is replaced by quartz with different particle sizes. The quartz used in AASQ 35, AASQ 60 and AASQ 130 has a d_{50} of 35 μm, 60 μm and 130 μm, respectively.

those between AASF pastes made from different fly ashes. This information indicates the role of fly ash in AASF paste is not the same as quartz, but treating the fly ash as quartz will not lead to a misestimation of reaction kinetics larger than that induced by using different batches of fly ash.

As shown in Fig. 6(b), AASQ pastes generated nearly the same total heat as the AASF1 pastes at 1 week, irrespective of the particle size of the quartz. Therefore, from the aspects of reaction kinetics and reaction degree in the first 7 days, the role of fly ash in AASF systems seems similar, although not identical, to that of a filler like quartz. Therefore, the replacement of half of the slag by fly ash should not result in a different shrinkage mechanism of the material under ambient condition.

3.2.4. Pore structure

The pore volume and pore size distribution of AAS and AASF pastes characterized by nitrogen absorption are shown in Fig. 7. At the age of 1 day, the total pore volume in AAS is higher than in AASF due to a faster formation of gel structures in AAS paste. AAS paste show critical pore size at around 4.5 nm and 20 nm at this age, while AASF paste does not show characteristic pores within the measuring range of nitrogen absorption. This indicates that a dense microstructure have not formed yet in AASF pastes. After 7 days, a critical pore size of 3.5 nm can be identified for AAS, indicating the formation of a large amount of gel pores [58]. Compared with AAS, AASF shows coarser gel pores, with the critical pore size at around 5 nm, and a larger total porosity. The coarser pore structure when slag is replaced by fly ash is consistent with the findings from the literature [25,59] and also with the cumulative heat release results shown in Fig. 6. The denser pore structure of AAS paste may contribute to a smaller radius of the menisci formed within the paste, which can lead to a larger pore pressure that can generate autogenous shrinkage. This point will be confirmed in Section 3.4.

By summarizing the characterization results shown above, it can be found that AAS and AASF systems have the same type of reaction products. The substitution of slag by fly ash leads to a lower reaction degree of the paste and a coarser microstructure. Consequently, the magnitude of the driving force of the autogenous shrinkage and the deformability of the pastes would be different. In the following sections, the driving forces of the autogenous shrinkage and the deformability of the pastes will be investigated.

3.3. Chemical shrinkage

Chemical shrinkage is believed to be the primary reason for self-desiccation in OPC based systems [60,61]. Since the total volume of hydration products is smaller than the volume of reactants (cement and water) [62], internal voids would form when the paste is stiff enough. As a result, negative pore pressure and autogenous shrinkage of the paste are generated [63]. To confirm that AAMs follow similar mechanisms, the chemical shrinkage of AAS and AASF is measured, as shown in Fig. 8.

It can be seen from Fig. 8 (a) that both AAS and AASF pastes show chemical shrinkage after final setting (35 min for AAS paste and 103 min for AAFS paste). The chemical shrinkage of AAS is a bit smaller than that of OPC at the same curing age. The lower chemical shrinkage of AASF paste than AAS paste is consistent with the lower reaction degree of AASF indicated by the cumulative reaction heat results as shown in Fig. 5(b). However, the chemical shrinkages of the two pastes are rather similar in the unit of ml per gram of slag, as shown in Fig. 8(b). This verifies the hypothesis proposed above that the slag dominates the reactions in AASF at ambient condition. At the age of 7 days, AASF shows a slightly higher chemical shrinkage (ml/g slag) than AAS, which may be due to the higher reaction degree of slag in AASF system than in AAS system (see [64]) and the reaction of the amorphous phase in fly ash.

The chemical shrinkage of the two pastes indicates that internal voids are formed in the systems and the pore pressure generated by liquid-gas menisci will be one of the driving forces of the autogenous shrinkage.

3.4. Internal RH and pore pressure

In order to confirm the occurrence of self-desiccation in AAMs and quantify the pore pressure, the internal RH of the pastes is measured. The RH that indicates the curvature effect of the meniscus can be calculated according to Eq. (1) [65].

$$RH = RH_S \cdot RH_K \quad (1)$$

where RH is the (measured) relative humidity of the paste, RH_S is due to the dissolved salts in the pore fluid and RH_K is due to meniscus formation in a circular cylindrical pore.

Fig. 9 shows the measured RH of AAS and AASF pastes and RH_S of the pore fluid. The calculated RH_K is also shown in Fig. 9. It can be seen that the RH_S of the pore solutions of the pastes is lower than 100% due to the presence of ions. The similar RH_S values (around 95%) of AAS and AASF indicate similar ions concentrations in the pore solutions. Both AAS and AASF show a decrease in RH_K, indicating the occurrence of self-desiccation in the paste. The RH_K drop in AAS is more evident than in AASF.

The extents of RH_K drop in AAS and AASF paste can be explained according to Kelvin equation (Eq. (2)).

$$\ln(RH_K) = \frac{2\gamma V_w}{rRT} \quad (2)$$

where γ (N/m) and V_w (m^3/mol) are the surface tension and the molar

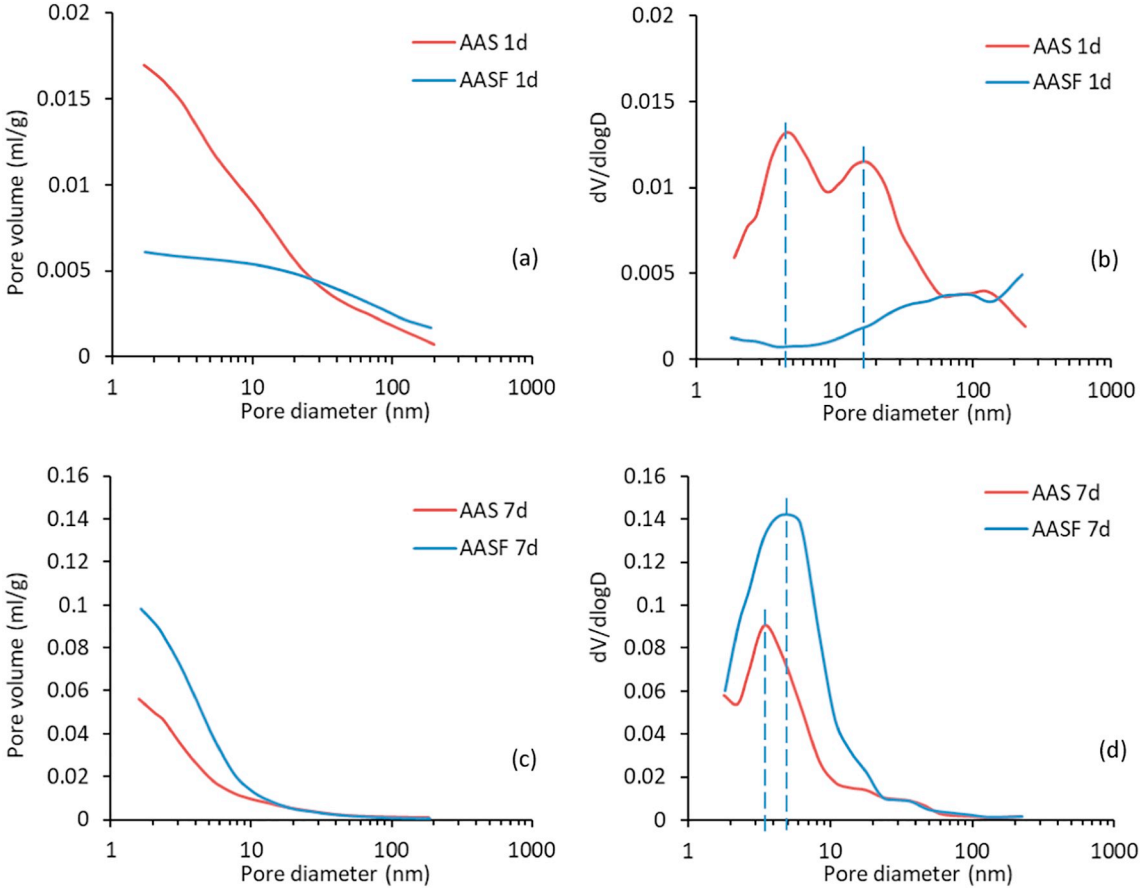

Fig. 7. Pore volume and differential curves for AAS and AASF cured for (a,b) 1 day and (c,d) 7 days.

volume of the pore solution, respectively; r (m) is the radius of the menisci; R (8.314 J/(mol·K)) is the ideal gas constant and T (K) is the absolute temperature, in this paper 293.15 K.

In Eq. (2), R and T are constants. According to Lura [61], the ions have limited effect on V_w. Thus the value of V_w can be considered as a constant and taken as that for water, i.e. 18.02 × 10^{-6} m^3/mol. Then, it is the surface tension of the pore solution and the menisci radius that control the RH_K. The surface tensions of the pore solutions of AAS and AASF are believed to be similar due to the similar ions concentrations indicated by the RH_S results [60]. According to Figs. 7 and 8, AAS paste shows higher chemical shrinkage and higher extent of pore refinement than AASF paste, therefore, the diameter of menisci in AAS is supposed to be smaller [60], which qualitatively explains the severer RH_K drop in AAS paste compared to AASF paste.

Combining Kelvin equation (Eq. (2)) and Laplace equation (Eq. (3)), the pore pressure σ (MPa) induced by the drop of RH_K can be calculated by Eq. (4).

$$\sigma = -\frac{2\gamma}{r} \tag{3}$$

$$\sigma = -\frac{ln(RH_K)RT}{V_w} \tag{4}$$

The calculated pore pressure for AASF and AAS at the age 1 day, 3 days and 7 days is shown in Fig. 10. It can be seen that larger pore

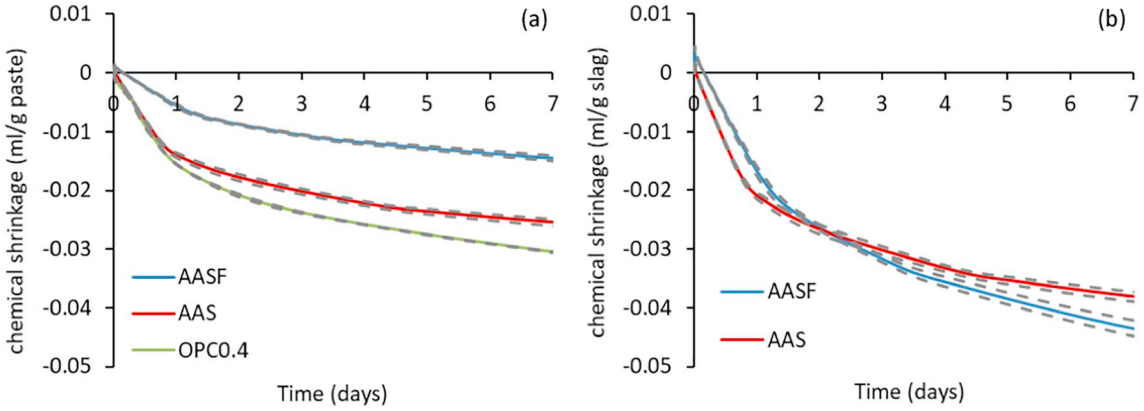

Fig. 8. (a) Chemical shrinkage of AAS and AASF pastes in comparison with that of OPC paste, in ml per gram of paste and (b) chemical shrinkage of AAS and AASF paste in ml per gram of slag. The results of the two replicates for each mixture are shown in dashed lines while the average data is shown in solid line.

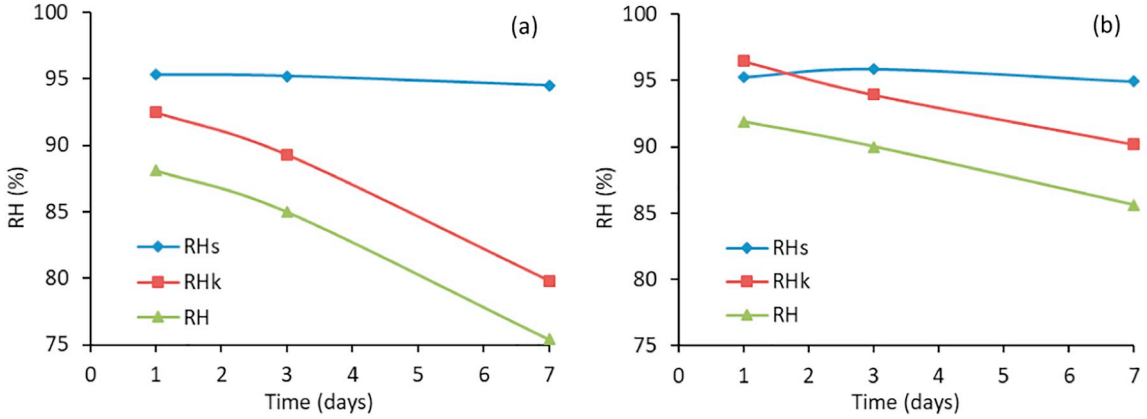

Fig. 9. Internal RH results of AAS (a) and AASF (b). RH is the measured RH of the paste, RH_S is due to the dissolved salts in the pore solution and RH_K is due to the curvature effect of the liquid-gas menisci as calculated with Eq. (1).

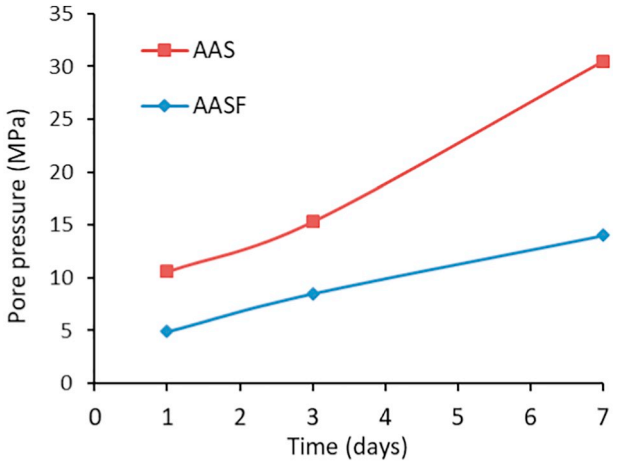

Fig. 10. Calculated pore pressure in AAS and AASF according to Eq. 4.

pressure is generated in AAS than in AASF, which contributes to the larger autogenous shrinkage of AAS paste.

Compared with the published results (e.g. Fig. 5.9 in [61] and Fig. 5.8 in [66]), the pore pressure generated in AASF paste is around two times higher than that in OPC paste with a w/c of 0.4. This might be one of reasons why AASF shows larger autogenous shrinkage than OPC0.4 (see Fig. 2). However, the two times larger pore pressure may not fully explain the 6 times larger autogenous shrinkage of AASF compared to OPC0.4. It is therefore suspected that other driving forces besides the pore pressure induced by self-desiccation may also exist. More information on this will be given in next section.

3.5. Shrinkage under saturated condition

To verify the existence of other driving force besides pore pressure, the autogenous shrinkage of AAS and AASF pastes under saturated condition is measured, as shown in Fig. 11. The results are compared with the deformation (i.e., autogenous shrinkage) of the pastes under sealed condition.

It can be seen from Fig. 11(c) that OPC0.4 shows expansion under saturated condition. This phenomenon is attributed to the absence of capillary tension and the formation of crystals (e.g. ettringite) that exert pressure on the microstructure [42,67]. By contrast, AAS and AASF show a noticeable shrinkage even under saturated condition, especially in the first day. This finding is in consistency with the results obtained by Yang et al. [68], who observed considerable shrinkage of AAS cured in an environment with RH above 90%. After the age of 1 day, the shrinkage of AAM pastes under saturated condition develops much slower. A similar trend on AAS mortar was observed by Palacios and Puertas [69]. The results in Fig. 11 indicate that besides self-desiccation, there is other driving force that can induce autogenous shrinkage of AAMs, especially at early age.

Several studies proposed the possibility of existence of other mechanisms of autogenous shrinkage of AAMs other than self-desiccation. For example, Fang et al. [22] found that a large part of the early age autogenous shrinkage of AASF is associated with the development of chemical shrinkage, however, they did not define the driving force behind. Uppalapati and Cizer [21] hypothesized that the autogenous shrinkage of AAS is related to the polymerization reaction during forming C-A-S-H gel. However, this mechanism cannot explain the different autogenous shrinkage behaviors of AAS and OPC, since the polymerization degree of Si in C-A-S-H (mostly in the form of Q^2 [70,71]) is actually similar to that of Si in C-S-H.

In the sub-micro level, several forces are involved between the gel surfaces, including attractive forces, e.g., van der Waals force, and impulsive forces, e.g., double-layer force and steric-hydration force [72,73]. DLVO theory (named after Derjaguin, Landau, Verwey and Overbeek [74,75]) provides a framework for the balance between van der Waals force and double-layer force [76,77]. However, for separations below about 5 nm and for concentrated solutions (10^{-2}–10^{-1} M) especially when divalent or multivalent ions, e.g., Ca^{2+}, Al^{3+}, and SiO_3^{2-}, are present in the electrolytic solution, DLVO theory was also found unable to interpret the interparticle forces [77–80]. In these situations, non-DLVO forces such as the steric-hydration force play more important roles. The steric-hydration force is an impulsive force generated by the hydration shells surrounding individual ions. In the electrolytic solution, ions (especially divalent ions) would absorb neighbouring water molecules to form hydration shells and the counter overlap of the shells of individual ions would provide strong repulsive steric force to avoid the solid surfaces reaching closer [81]. As reported in [72,77], the repulsive hydration force is stronger than either of the two DLVO forces.

In AAMs systems, there are large amounts of ions such as Na^+, OH^- and SiO_3^{2-} in the initial pore solution. The hydration shells within the interstitial space counterbalance the attractive forces between gel particles to resist the densification of the gel structure. From the start of the acceleration period, the reaction is progressing rapidly and the concentrations of ions decrease dramatically. For example, the concentration of SiO_3^{2-} in similar AAM systems decreases from > 2 M to 100–200 mM according to [48,82]. The reduced concentrations of the ions and the hydration shells substantially lead to a reduction of the steric-hydration force, while the attractive forces like van der Waals force remain unchanged. As a result, the gel particles surrounding the pores approach closer to each other, which expressed as a rearrangement or densification of the gel [19]. This effect together with the

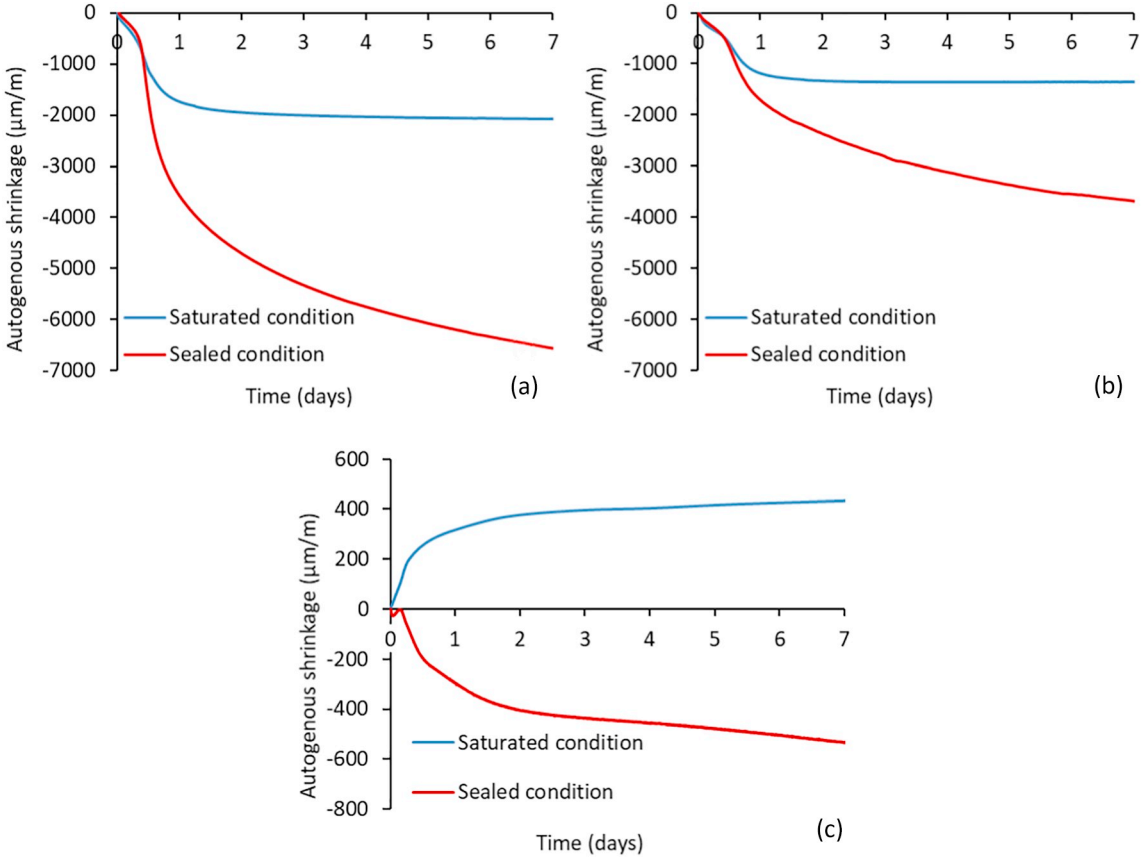

Fig. 11. Shrinkage of AAS (a), AASF (b) and OPC0.4 (c) under saturated condition in comparison with the autogenous shrinkage (under sealed condition).

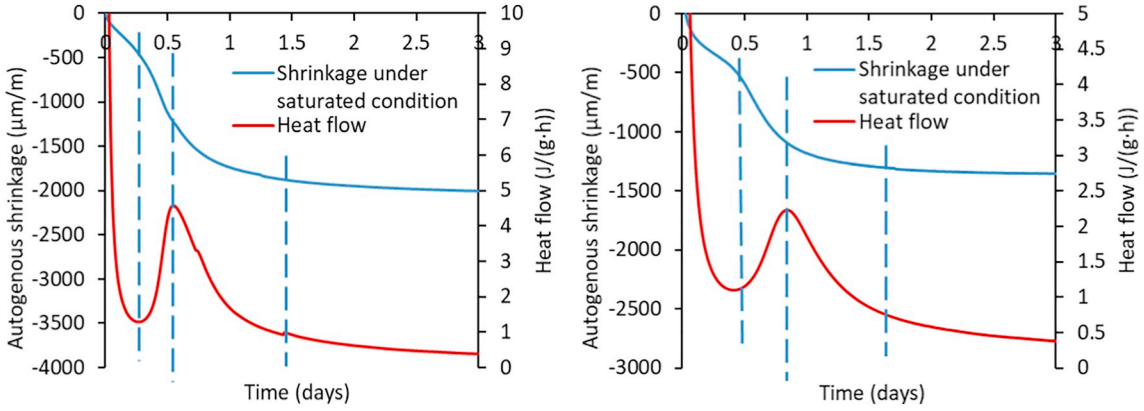

Fig. 12. Shrinkage of AAS (a) and AASF (b) under saturated condition, plotted together with the reaction heat.

continuous formation of new products contributes to the formation of a denser and stronger skeleton (see Fig. 7). The correlation between the shrinkage under saturated condition and the reaction heat of AAS and AASF is presented in Fig. 12. The larger shrinkage of AAS than AASF might be due to the faster reaction in AAS in the acceleration period.

After the acceleration period, the reactions slow down and the concentrations of the ions become stable [82], hence the steric-hydration force also stabilizes. As a result, AAS and AASF show little shrinkage under saturated condition in the deceleration period, as shown in Fig. 12. For the samples in sealed condition, the autogenous shrinkage keeps increasing after the acceleration period due to the increasing pore pressure (see Fig. 2).

The mechanism proposed above is a possible explanation of the shrinkage of AAS and AASF under saturated condition. This kind of shrinkage was not observed in OPC for two reasons. First, the ion concentrations in the pore solution of OPC are much lower than in alkali-activated systems and are relatively stable during the acceleration and subsequent periods [83,84]. Second, the shrinkage induced by steric-hydration force, if any, can be compensated by the expansion of the paste after final setting caused by the formation of crystals, e.g. ettringite [67]. The existence of mechanism of the autogenous shrinkage of AAMs other than self-desiccation explains why the autogenous shrinkage of AAS cannot be entirely mitigated by internal curing (see the results in [85]). Future study is needed to quantify the decrease of steric-hydration force in different reaction processes.

3.6. Elastic modulus evolution

The elastic modulus of AAS and AASF determined by EMM-ARM is shown in Fig. 13. It is seen that the elastic modulus of AAS and AASF

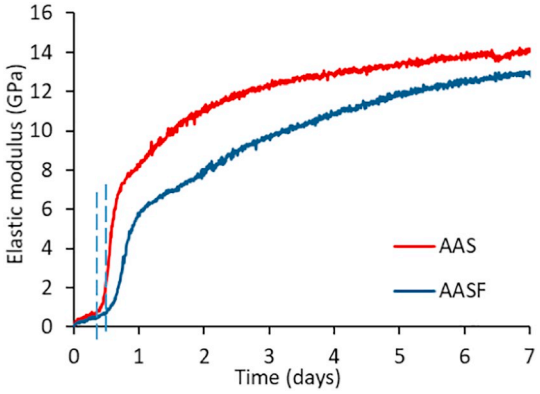

Fig. 13. Evolution of elastic modulus of AAS and AASF paste. The dashed line indicates the instants when the elastic modulus starts to rapidly increase.

remains at a low level at the dormant period (until 8 h for AAS and 11 h for AASF, see Fig. 5(a)). After that, the elastic modulus of the two systems experiences a sudden increase. After 1 day when the reaction rate slows down, the elastic modulus of the two systems starts to develop at a lower speed. AAS shows higher elastic modulus than AASF after the dormant period due to the larger amount of reaction products and the denser pore structure formed in the paste as shown in Section 3.2. The elastic modulus of AAMs is slightly lower than that of OPC paste made from similar water/binder ratios according to the results reported in [61,86].

A phenomenon different from what has been observed in OPC systems is that the elastic modulus of AAMs starts to rapidly develop at the start of the acceleration period, which is far beyond the final setting time (see Table 3). For OPC, the final setting time normally indicates the formation of solid percolation, when the reaction products surrounding the cement particles start forming a solid cluster that spans the whole sample [87]. Therefore, the elastic modulus of OPC was observed to rapidly increase after the final setting [38]. For AAMs, in contrast, the final setting is probably the result of flowability loss of the paste due to the formation of initial products from the alkali and silicate ions in the interstitial space [88]. At such a short time (within 1 h after mixing), a solid skeleton with enough stiffness has not formed yet.

This finding is actually consistent with the shrinkage data. As can be seen from Fig. 11(a) and (b), the shrinkages are the same under different conditions in the dormant period, which indicates that no considerable pore pressure is generated in sealed cured AAMs in this stage. Otherwise, the autogenous shrinkage of AAMs under sealed condition should be higher than the shrinkage under saturated condition. As the chemical shrinkage progresses, the liquid should have started to be consumed in the dormant period, but the paste is not stiff enough to resist a large pore pressure and can generate pronounced bulk deformation to compensate the formation of menisci. Therefore, the shrinkage in this stage is likely to be viscous or even plastic deformation that is converted from chemical shrinkage. An important support for this finding can be found in a previous study [85], which showed that the restrained autogenous shrinkage of AAS paste generates stress only after the dormant period. This finding is also in agreement with the results obtained by Ma et al. [89], who measured the internal pore pressure in AAMs and found that the pore pressure starts to develop only after the dormant period. Therefore, it seems that the starting point of the acceleration period is a better indication of the "time-zero" of the autogenous shrinkage of AAMs.

3.7. Modelling of the autogenous shrinkage

In this section, results of early-age properties of AAM pastes, presented in previous sections, are used as inputs for calculating autogenous shrinkage of AAS and AASF pastes. Based on the analyses above, the autogenous shrinkage of AAMs can be divided into two parts (Eq. (5)), the part induced by pore pressure and the part induced by other driving forces like steric-hydration force.

$$\varepsilon_{AS} = \varepsilon_{pore} + \varepsilon_{ste} \tag{5}$$

ε_{ste} can be experimentally measured under saturated condition, as shown in Fig. 11.

ε_{pore} can be considered as the sum of two parts, namely the elastic part and the non-elastic/creep part, as shown in Eq. (6). The starting point of the acceleration period instead of final setting time is used as the time-zero of the autogenous shrinkage in the calculations below.

$$\varepsilon_{pore} = \varepsilon_{elas} + \varepsilon_{creep} \tag{6}$$

According to Bentz et al. [90], the elastic deformation of the paste induced by pore pressure can be calculated by Eq. (7).

$$\varepsilon_{elas} = \frac{S\sigma}{3}\left(\frac{1}{K} - \frac{1}{K_S}\right) \tag{7}$$

where S (m^3 liquid/m^3 pore) is the saturation fraction; σ (MPa) is the stress in the pore solution calculated by Eq. (4); K (MPa) is the bulk modulus of the paste and K_S (MPa) is the bulk modulus of the solid material.

The saturation fraction S can be calculated as the ratio between the liquid content in the hardening paste, V_l (ml), and the total pore volume of the paste, V_p (ml), which can be calculated according to the initial liquid content, V_{il} (ml), the non-evaporable liquid content, V_{nl} (ml), and the chemical shrinkage, V_{cs} (ml), according to Eq. (8) [61]. The detailed procedure to determine V_{nl} (ml) was described in [48].

$$S = \frac{V_l}{V_p} = \frac{V_{il} - V_{nl}}{V_{il} - V_{nl} + V_{cs}} \tag{8}$$

The calculated saturation fractions of the pastes are shown in Table 4. In general, AAS shows lower saturation fraction than AASF and the saturation fraction of the two systems decrease with reaction time.

The bulk modulus K of AAS and AASF pastes is calculated with Eq. (9):

$$K = \frac{E}{3(1 - 2\upsilon)} \tag{9}$$

where E (GPa) is the elastic modulus and υ is the Poisson's ratio (−).

The elastic modulus results can be found in Fig. 13. The Poisson's ratio of AAS and AASF pastes is taken as 0.2 according to [91]. The bulk modulus K_S is taken as 44 GPa [92]. According to Lura [61], the variation of K_S has limited effect on the calculated shrinkage. Changing the value of K_S from 40 to 50 GPa results in a deviation of only 2% in the calculated shrinkage.

The elastic part of autogenous shrinkage induced by pore pressure is calculated and shown in Fig. 14. The elastic deformation between the age 1 day and 7 days are obtained by linear interpolation. It can be seen that the elastic deformation (ε_{elas}) only accounts for a small part of the total autogenous shrinkage.

To calculate the creep part of the autogenous shrinkage of AAMs, the available models developed for OPC systems is applied, as shown in Eq. (10). According to van Breugel [93], the creep of a cementitious material at time t can be calculated with Eq. (11), where the water/solid ratio and the reaction degree are two main parameters.

$$\varepsilon_{creep}(t,\tau) = \varepsilon_{elas}(\tau)\varphi(t,\tau) \tag{10}$$

Table 4.
Saturation fraction of AAS and AASF pastes.

Mixture	AAS 1d	AAS 7d	AASF 1d	AASF 7d
S	0.933	0.881	0.974	0.931

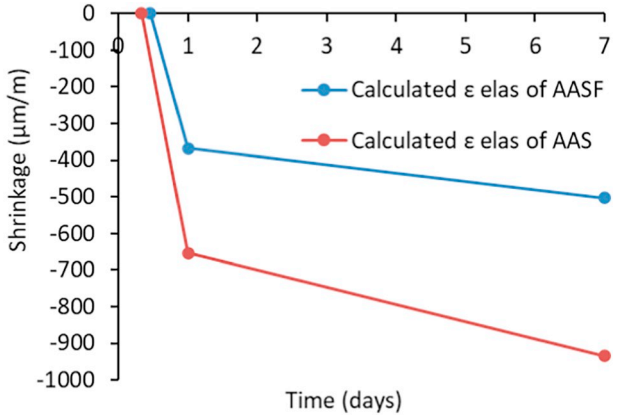

Fig. 14. Calculated ε_{elas} of AAS and AASF paste. The time-zero of the curves is the start of the acceleration period of the paste (8 h and 12 h for AAS and AASF, respectively).

where $\varphi(t,\tau)$ is the creep factor. τ (days) is the time when the load is applied.

$$\varphi(t,\tau) = \left(\frac{\alpha(t)}{\alpha(\tau)} - 1\right) + 1.34 * \omega^{1.65}\tau^{-d}(t-\tau)^{n}\frac{\alpha(t)}{\alpha(\tau)} \quad (11)$$

where α is the degree of reaction; ω is the water-solid ratio (0.344, see Table 2); n is the relaxation factor which value is taken as 0.3 and d is the constant which value is taken as 0.35 [94].

The reaction degree term $\frac{\alpha(t)}{\alpha(\tau)}$ can be calculated by Eq. (12). The reaction heat results have been shown in Fig. 5.

$$\frac{\alpha(t)}{\alpha(\tau)} = \frac{Q(t)}{Q(\tau)} \quad (12)$$

where $Q(t)$ and $Q(\tau)$ are the reaction heats of the paste at time t and τ.

Since the pore pressure is increasing with time, the creep part of the autogenous shrinkage at a certain age needs to be considered as the accumulation of increments of creep deformations that formed at previous time, e.g. from τ_1 to τ_{n-1}. Within each time interval, the load can be treated as constant. Therefore, the creep induced by pore pressure can be calculated by Eq. (13).

$$\varepsilon_{creep} = \sum_{k=1}^{n-1} \Delta\varepsilon_{elas}(\tau_k)\left(\left(\frac{\alpha(t)}{\alpha(\tau_k)} - 1\right) + 1.34 * \omega^{1.65}\tau_k^{-d}(t-\tau_k)^{n}\frac{\alpha(t)}{\alpha(\tau_k)}\right) \quad (13)$$

where $\Delta\varepsilon_{elas}(\tau_k)$ is the increment of elastic deformation from τ_{k-1} to τ_k.

A schematic representation of the calculation process mentioned above is shown in Fig. 15.

Based on the Equations above, the creep part of the autogenous shrinkage induced by pore pressure (ε_{creep}) is calculated and compared with ε_{elas}, as shown in Fig. 16. It can be seen that ε_{creep} of AAMs is more than three times higher than ε_{elas}, especially at later age. For plain OPC paste, the creep part was generally reported to be with a similar magnitude to that of the elastic part of the autogenous shrinkage. For OPC paste blended with fly ash or slag, the creep coefficient (creep part/elastic part) can reach 2 [12,61,66]. Hence, it seems that AAM systems show more evident viscosity than OPC based systems. This finding is in line with the evident creep/relaxation of AAM paste and concrete reported by Ye and Radlińska [19], Li et al. [95] and Kostiuchenko et al. [96]. According to [19], the evident viscous deformation of AAMs is due to the rearrangement of C-A-S-H gel. The reason why C-A-S-H gel is more viscoelastic compared with C-S-H gel lies in the structural incorporation of alkali cations in C-A-S-H, which reduces the stacking regularity of C-A-S-H layers and makes the gel easier to collapse and redistribute [19].

With the calculated ε_{elas} and ε_{creep}, and the measured ε_{ste}, the total autogenous shrinkage can be calculated by combining Eqs. (5) and (6). The calculated autogenous shrinkage of the pastes is compared with the measured one as shown in Fig. 17.

In Fig. 17, the calculated autogenous shrinkage curves of AAM paste agree fairly well with the measured ones, especially for AAS paste. This also confirms the hypothesis of the autogenous shrinkage mechanism proposed in this study. The results also indicate that the creep model developed in [93] for OPC based systems can also be used to predict the pore pressure induced-creep of AAMs.

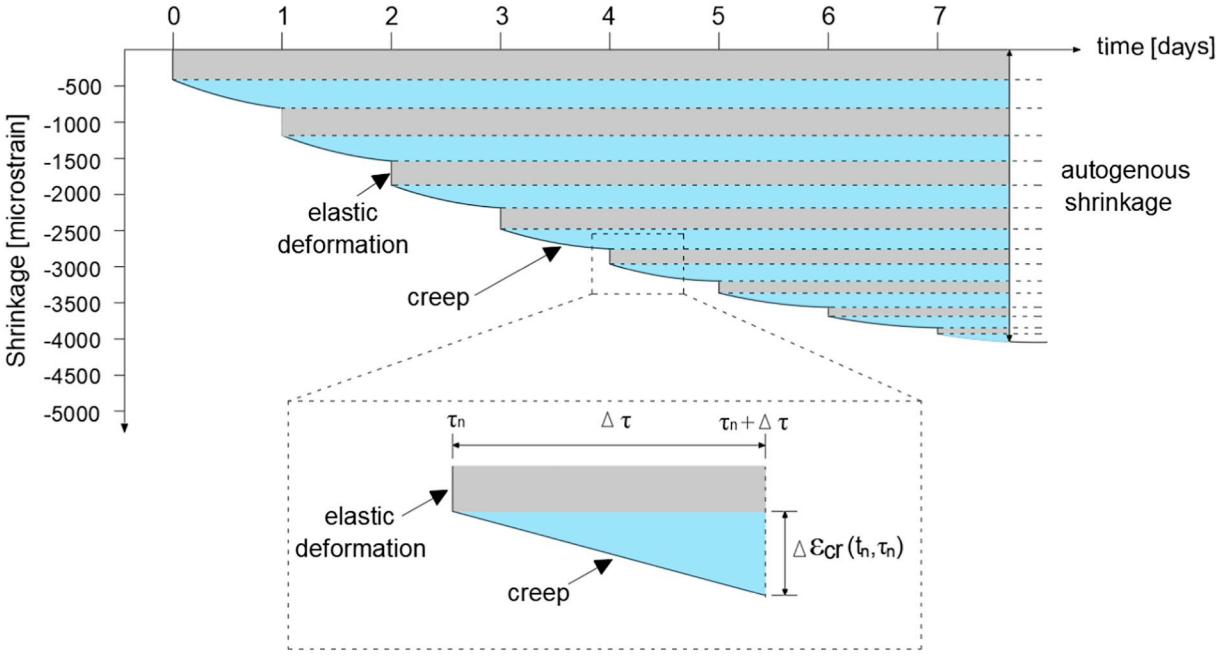

Fig. 15. Schematic representation of pore pressure induced autogenous shrinkage of the paste, after [66].

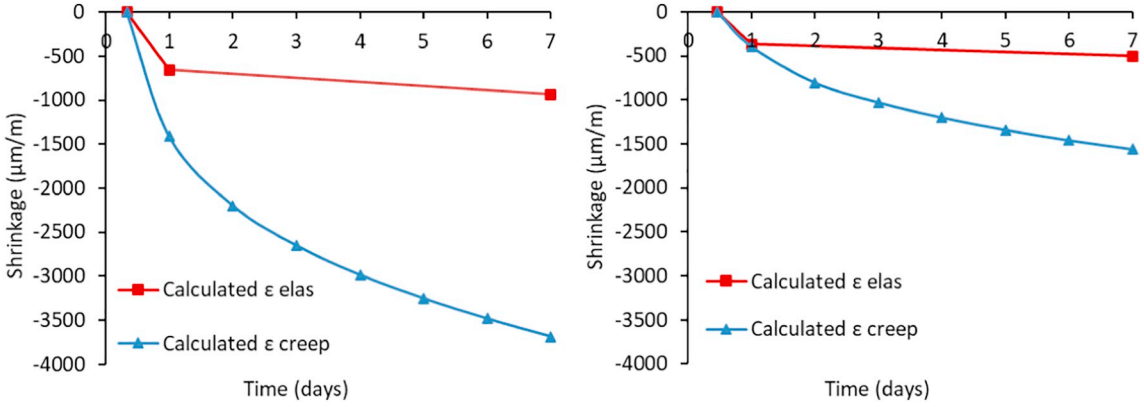

Fig. 16. Calculated ε_{creep} of AAS (a) and AAASF (b) paste, in comparison with ε_{elas}. The time-zero of the curves is 8 h and 11 h for AAS and AASF, respectively.

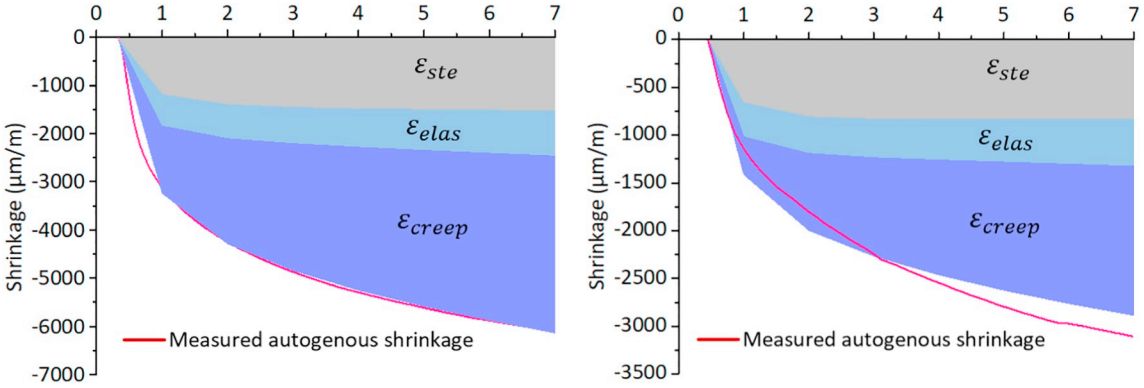

Fig. 17. Calculated and measured autogenous shrinkage of AAS paste (a) and AASF paste (b).

At the age of 1 day, the calculated ε_{AS} slightly underestimates the autogenous shrinkage of AAS paste and slightly overestimates the one of AASF paste. The reason probably lies in the Poisson's ratio values assumed in the modelling. Compared with activator and raw materials, the reaction products (C-A-S-H gel) with locally porous structure normally show lower Poisson's ratio [97]. According to the results in Section 3.2, AAS has higher reaction degree and a larger amount of reaction products formed compared to AASF, especially at 1 day. Therefore, the real Poisson's ratio of AAS paste should be lower than that of AASF at that time. In the modelling, however, the value 0.2 was assumed for both pastes, which may lead to an overestimation of the real Poisson's ratio for AAS and an underestimation for AASF. As a result, the ε_{pore} of AAS is underestimated and the one of AASF is overestimated. From 1 day to 6 days, there is a small discrepancy between the calculated ε_{AS} of AASF and the measured curve, which may be because the calculated ε_{elas} in this period is obtained by linear interpolation.

This section provides a useful strategy for academia and industrial users to predict the autogenous shrinkage of AAMs. The important input parameters that need to be known are: internal RH, saturation fraction, elastic modulus, reaction heat evolution and shrinkage under saturated condition (ε_{ste}). The good agreement between the calculated and the measured autogenous shrinkage of AAMs, in turn, verifies the mechanism identified in this study. It might also be interesting to check whether the existing models in standards for OPC can be used to predict the autogenous shrinkage of AAMs. An example is given in Appendix A, which shows the autogenous shrinkage of AAS and AASF is greatly underestimated with the models in *fib* Model Code 2010. Shrinkage-predicting models based on fundamental descriptions of the reaction and microstructures of AAMs need future research.

4. Concluding remarks

In this study, the autogenous shrinkage of AAS and AASF pastes is measured and the mechanisms of the autogenous shrinkage are investigated. The role of fly ash in AASF paste is clarified. A model for calculating the autogenous shrinkage of AAMs is proposed. The autogenous shrinkage of AAMs is then calculated and compared with the measured results. The following remarks can be made:

1. AAM pastes show larger autogenous shrinkage than OPC paste. The more slag used in the precursor, the larger autogenous shrinkage of the AAM pastes.
2. The main reaction products in AAS and AASF are C-A-S-H type gel. Compared with AAS, AASF shows a longer dormant period, a smaller amount of reaction products and a coarser pore structure at the first 7 days. From the early-age reaction kinetics point of view, the role of fly ash is similar to that of inert filler.
3. In the dormant period, the stiffness of the paste remains low and the autogenous shrinkage is mainly viscous/plastic deformation. From the start of the acceleration period, the elastic modulus of the paste increases rapidly and the pore pressure starts to develop due to drastic drop of internal RH. No significant change in the reaction kinetics or stiffness evolution is observed around the final setting time determined by Vicat needle. It is therefore suggested that the moment when the acceleration period starts is a more proper

indication of the time-zero for the autogenous shrinkage of AAMs than the Vicat final setting time.
4. For the first time, it is confirmed that self-desiccation is not the only mechanism of autogenous shrinkage of AAMs. Besides self-desiccation, it is believed that the reduction of steric-hydration force due to the significant consumption of ions also induces a certain amount of shrinkage, especially in the acceleration period. In the deceleration period, pore pressure becomes the dominant driving force of the autogenous shrinkage.
5. AAS and AASF pastes show pronounced viscoelasticity in comparison with OPC paste. Creep deformation under the load of pore pressure plays an important role in the autogenous shrinkage of AAMs.
6. A computational model is proposed to estimate the autogenous shrinkage of AAMs pastes based on the mechanisms clarified. By summing the shrinkage under saturated condition, the elastic and creep shrinkage induced by the pore pressure, the calculated autogenous shrinkage agrees very well with the measured results.

CRediT authorship contribution statement

Zhenming Li:Conceptualization, Methodology, Software, Investigation, Writing - original draft, Writing - review & editing.**Tianshi Lu**:Conceptualization, Software, Methodology.**Xuhui Liang**: Methodology, Investigation.**Hua Dong**:Methodology, Writing - review & editing.**Guang Ye**:Supervision, Writing - review & editing.

Declaration of competing interest

The authors declare that they have no conflict of interest.

Acknowledgment

Zhenming Li and Xuhui Liang would like to acknowledge the funding supported by the China Scholarship Council (CSC) under grant No. 201506120072 and No. 201806050051. This work is supported also by the grant from the Netherlands Organisation for Scientific Research (NWO). Klaas van Breugel is acknowledged for the discussion on the modelling. Dr. Xiaowei Ouyang and Dr. Yibing Zuo are acknowledged for the discussions on the autogenous shrinkage mechanisms.

Appendix A

Currently, there is no standard model to predict the autogenous shrinkage of AAMs. It is interesting to know whether the analytical models for OPC can be used to predict the autogenous shrinkage of AAMs. Herein, the model from *fib* Model Code 2010 is tentatively used to calculate the autogenous shrinkage of AAS and AASF pastes, as shown in Eq. A.1. However, it should be noted that Eq. A.1 as well as other standard models concern mainly on the autogenous shrinkage of concrete rather than paste. Corrections on the data are needed afterwards

$$\varepsilon_c(t) = \varepsilon_{aso}(f_{cm}) \bullet \beta_{as}(t) \tag{A.1}$$

where $\varepsilon_c(t)$ is the autogenous shrinkage of concrete; f_{cm} is the mean compressive strength of concrete at an age of 28 days, which is 91.4 MPa and 75.2 MPa for AAS and AASF concrete, respectively [98]; $\varepsilon_{aso}(f_{cm})$ is the notional autogenous shrinkage coefficient and can be expressed as:

$$\varepsilon_{aso}(f_{cm}) = -\alpha_{as}\left(\frac{f_{cm}/10}{6 + f_{cm}/10}\right)^{2.5} \bullet 10^{-6} \tag{A.2}$$

where α_{as} is a coefficient which depends on the type of cement; $\alpha_{as} = 800$ for slowly hardening cements, $\alpha_{as} = 700$ for normal or rapidly hardening cements, $\alpha_{as} = 600$ for rapidly hardening high-strength cements. Considering the short setting time and high strength of AAS and AASF, the coefficient α_{as} is chosen as 600.

The factor $\beta_{as}(t)$ in Eq. A.1 describes the relationship between the autogenous shrinkage and time and it can be written as:

$$\beta_{as}(t) = 1 - exp(-0.2 \bullet t^{0.5}) \tag{A.3}$$

From the calculated autogenous shrinkage of the concrete ε_c, the autogenous shrinkage of the paste ε_p can be obtained according to reduced Hobbs' model [99], as shown in Eq. A.4 [100].

$$\frac{\varepsilon_c}{\varepsilon_p} = \frac{1 - \phi_A}{1 + \phi_A} \tag{A.4}$$

where ϕ_A is the volume fraction of aggregates, 67% [98].

The accordingly calculated autogenous shrinkage of AAS and AASF paste based on *fib* Code 2010 is shown in Fig. A.1, in comparison with the experimentally measured results. It can be seen the predicted results by *fib* models used for OPC with the compressive strength of AAMs as inputs substantially underestimate the autogenous shrinkage of AAS and AASF paste. One may argue that the utilization of Hobbs' model to consider the influence of aggregates may lead to error in the prediction of the shrinkage of paste. However, the error caused by using Hobbs' model cannot explain the discrepancy as large as shown in Fig. A.1. The huge discrepancy between the calculated and the measured autogenous shrinkage of AAMs paste indicates that the analytical models involving empirical parameters for OPC systems are not applicable for AAMs. The different shrinkage mechanisms of these two types of materials need to be emphasized in future development of shrinkage-prediction models.

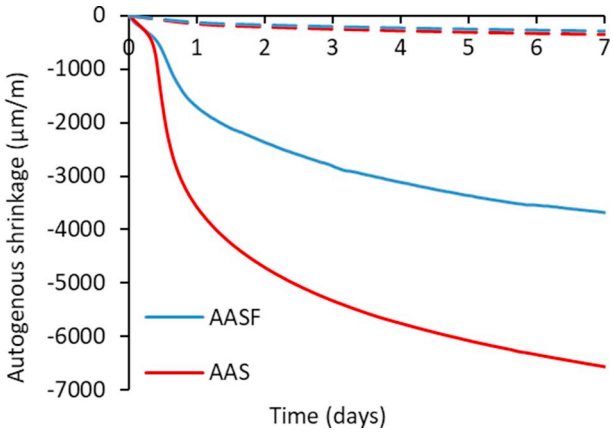

Fig. A.1. Calculated based on *fib* Code 2010 (dashed lines) and measured (solid lines) autogenous shrinkage of AAS and AASF pastes.

References

[1] J.L. Provis, Alkali-activated materials, Cem. Concr. Res. 114 (2018) 40–48, https://doi.org/10.1016/j.cemconres.2017.02.009.

[2] R.J. Thomas, H. Ye, A. Radlinska, S. Peethamparan, Alkali-activated slag cement concrete, Concr. Int. 38 (2016) 33–38.

[3] P. Duxson, J.L. Provis, G.C. Lukey, J.S.J. van Deventer, The role of inorganic polymer technology in the development of "green concrete", Cem. Concr. Res. 37 (2007) 1590–1597, https://doi.org/10.1016/j.cemconres.2007.08.018.

[4] C. Shi, A.F. Jiménez, A. Palomo, New cements for the 21st century: the pursuit of an alternative to Portland cement, Cem. Concr. Res. 41 (2011) 750–763, https://doi.org/10.1016/j.cemconres.2011.03.016.

[5] J.L. Provis, J.S.J. Van Deventer, Geopolymers: Structures, Processing, Properties and Industrial Applications, Woodhead, Cambridge, UK, 2009.

[6] K. Arbi, M. Nedeljković, Y. Zuo, G. Ye, A review on the durability of alkali-activated Fly ash/slag systems: advances, issues, and perspectives, Ind. Eng. Chem. Res. 55 (2016) 5439–5453, https://doi.org/10.1021/acs.iecr.6b00559.

[7] M.C.G. Juenger, F. Winnefeld, J.L. Provis, J.H. Ideker, Advances in alternative cementitious binders, Cem. Concr. Res. 41 (2011) 1232–1243, https://doi.org/10.1016/j.cemconres.2010.11.012.

[8] N. Marjanović, M. Komljenović, Z. Baščarević, V. Nikolić, R. Petrović, Physical-mechanical and microstructural properties of alkali-activated fly ash-blast furnace slag blends, Ceram. Int. 41 (2015) 1421–1435, https://doi.org/10.1016/j.ceramint.2014.09.075.

[9] M. Chi, R. Huang, Binding mechanism and properties of alkali-activated fly ash/slag mortars, Constr. Build. Mater. 40 (2013) 291–298, https://doi.org/10.1016/j.conbuildmat.2012.11.003.

[10] W. Shen, Y. Wang, T. Zhang, M. Zhou, J. Li, X. Cui, Magnesia modification of alkali-activated slag fly ash cement, J. Wuhan Univ. Technol. Mater. Sci. Ed. 26 (2011) 121–125, https://doi.org/10.1007/s11595-011-0182-8.

[11] J.G. Jang, N.K. Lee, H.K. Lee, Fresh and hardened properties of alkali-activated fly ash/slag pastes with superplasticizers, Constr. Build. Mater. 50 (2014) 169–176, https://doi.org/10.1016/j.conbuildmat.2013.09.048.

[12] Z. Hu, Early Hydration and Shrinkage of Alkali-Activated Slag/Fly Ash Blend Cement, Hunan University, 2013.

[13] A.M. Rashad, Properties of alkali-activated fly ash concrete blended with slag, Iran. J. Mater. Sci. Eng. 10 (2013) 57–64.

[14] F. Collins, J. Sanjayan, Effect of pore size distribution on drying shrinking of alkali-activated slag concrete, Cem. Concr. Res. 30 (2000) 1401–1406, https://doi.org/10.1016/S0008-8846(00)00327-6.

[15] H. Chen, M. Wyrzykowski, K. Scrivener, P. Lura, Prediction of self-desiccation in low water-to-cement ratio pastes based on pore structure evolution, Cem. Concr. Res. 49 (2013) 38–47, https://doi.org/10.1016/j.cemconres.2013.03.013.

[16] N.K. Lee, J.G. Jang, H.K. Lee, Shrinkage characteristics of alkali-activated fly ash/slag paste and mortar at early ages, Cem. Concr. Compos. 53 (2014) 239–248, https://doi.org/10.1016/j.cemconcomp.2014.07.007.

[17] B.D. Kumarappa, S. Peethamparan, M. Ngami, Autogenous shrinkage of alkali activated slag mortars: basic mechanisms and mitigation methods, Cem. Concr. Res. 109 (2018) 1–9, https://doi.org/10.1016/j.cemconres.2018.04.004.

[18] C. Cartwright, F. Rajabipour, A. Radli, Shrinkage characteristics of alkali-activated slag cements, J. Mater. Civ. Eng. 27 (2014) 1–9, https://doi.org/10.1061/(ASCE)MT.1943-5533.0001058.

[19] H. Ye, A. Radlińska, Shrinkage mechanisms of alkali-activated slag, Cem. Concr. Res. 88 (2016) 126–135, https://doi.org/10.1016/j.cemconres.2016.07.001.

[20] J. Ma, F. Dehn, Shrinkage and creep behavior of an alkali-activated slag concrete, Struct. Concr. 18 (2017) 801–810, https://doi.org/10.1002/suco.201600147.

[21] S. Uppalapati, O. Cizer, Understanding the autogenous shrinkage in alkali-activated slag/fly-ash blends, Int. Conf. ALKALI Act. Mater. GEOPOLYMERS VERSATILE Mater. Offer. HIGH Perform. LOW Emiss, 2018, p. 27.

[22] G. Fang, H. Bahrami, M. Zhang, Mechanisms of autogenous shrinkage of alkali-activated fly ash-slag pastes cured at ambient temperature within 24 h, Constr. Build. Mater. 171 (2018) 377–387, https://doi.org/10.1016/j.conbuildmat.2018.03.155.

[23] S. Aydin, A ternary optimisation of mineral additives of alkali activated cement mortars, Constr. Build. Mater. 43 (2013) 131–138, https://doi.org/10.1016/j.conbuildmat.2013.02.005.

[24] Y. Ma, G. Ye, The shrinkage of alkali activated fly ash, Cem. Concr. Res. 68 (2015) 75–82, https://doi.org/10.1016/j.cemconres.2014.10.024.

[25] M. Nedeljković, Carbonation Mechanism of Alkali-Activated Fly Ash and Slag Materials: In View of Long-Term Performance Predictions, Delft University of Technology, 2019.

[26] M. Nedeljković, Z. Li, G. Ye, Setting, strength, and autogenous shrinkage of alkali-activated Fly ash and slag pastes: effect of slag content, Materials (Basel) 11 (2018) 2121, https://doi.org/10.3390/ma11112121.

[27] Z. Li, M. Nedeljkovic, Y. Zuo, G. Ye, Autogenous shrinkage of alkali-activated slag-fly ash pastes, 5th Int. Slag Valoris. Symp., Leuven, 2017, pp. 369–372.

[28] ASTM C191-18a, Standard Test Methods for Time of Setting of Hydraulic Cement by Vicat Needle, (2019), pp. 1–8, https://doi.org/10.1520/C0191-18A.2.

[29] ASTM C1968, Standard Test Method for Autogenous Strain of Cement Paste and Mortar, (2013), pp. 1–8, https://doi.org/10.1520/C1698-09.2.

[30] Q. Tian, O.M. Jensen, Measurement with corrugated tubes of early-age autogenous shrinkage of cement-based materials, J. Chinese Ceram. Soc. 37 (2009) 39–45.

[31] Z. Li, P. Gao, G. Ye, Experimental study on autogenous deformation of metakaolin based geopolymer, 2nd Int. RILEM/COST Conf. Early Age Crack. Serv. Cem. Mater. Struct., Brussels, 2017, pp. 209–214.

[32] F. Puertas, T. Amat, A. Fernández-Jiménez, T. Vázquez, Mechanical and durable behaviour of alkaline cement mortars reinforced with polypropylene fibres, Cem. Concr. Res. 33 (2003) 2031–2036, https://doi.org/10.1016/S0008-8846(03)00222-9.

[33] D. Feng, A. Mikuni, Y. Hirano, R. Komatsu, K. Ikeda, Preparation of geopolymeric materials from Fly ash filler by steam curing with special reference to binder products, J. Ceram. Soc. Japan. 113 (2005) 82–86, https://doi.org/10.2109/jcersj.113.82.

[34] E.P. Barrett, L.G. Joyner, P.P. Halenda, The determination of pore volume and area distributions in porous substances. I. Computations from nitrogen isotherms, J. Am. Chem. Soc. 73 (1951) 373–380.

[35] ASTM C 1608, Standard Test Method for Chemical Shrinkage of Hydraulic Cement Paste, (2007), pp. 667–670.

[36] Z. Li, S. Zhang, Y. Zuo, W. Chen, G. Ye, Chemical deformation of metakaolin based geopolymer, Cem. Concr. Res. 120 (2019) 108–118, https://doi.org/10.1016/j.cemconres.2019.03.017.

[37] H. Huang, G. Ye, Examining the "time-zero" of autogenous shrinkage in high/ultra-high performance cement pastes, Cem. Concr. Res. 97 (2015) 107–114, https://doi.org/10.1016/j.cemconres.2017.03.010.

[38] M. Azenha, R. Faria, F. Magalhães, L. Ramos, Á. Cunha, Measurement of the E-modulus of cement pastes and mortars since casting, using a vibration based technique, Mater. Struct. Constr. 45 (2012) 81–92, https://doi.org/10.1617/s11527-011-9750-9.

[39] S. Uppalapati, Ö. Cizer, Assessing the autogenous shrinkage of alkali- activated slag/fly ash mortar blends, Am. Concr. Institute, ACI Spec. Publ, 2017 2017-Janua.

[40] G. Fang, W. Tu, Y. Zhu, M. Zhang, AUTOGENOUS SHRINKAGE OF ALKALI-ACTIVATED FLY ASH-SLAG PASTES WITH AND WITHOUT SAP, 4th Int. Conf. Serv. Life Des. Infrastructures, 2018, pp. 449–455.

[41] M. Ben Haha, G. Le Saout, F. Winnefeld, B. Lothenbach, Influence of activator type on hydration kinetics, hydrate assemblage and microstructural development of alkali activated blast-furnace slags, Cem. Concr. Res. 41 (2011) 301–310, https://doi.org/10.1016/j.cemconres.2010.11.016.

[42] M.D. Cohen, Theories of expansion in sulfoaluminate-type expansive cements: schools of thought, Cem. Concr. Res. 13 (1983) 809–818.

[43] W.K.W. Lee, J.S.J. van Deventer, Use of infrared spectroscopy to study geopolymerization of heterogeneous amorphous aluminosificates, Langmuir 19 (2003)

8726–8734, https://doi.org/10.1021/La026127e.
[44] I. Garcia-Lodeiro, A. Palomo, A. Fernández-Jiménez, D.E. MacPhee, Compatibility studies between N-A-S-H and C-A-S-H gels. Study in the ternary diagram Na2O-CaO-Al2O3-SiO2-H2O, Cem. Concr. Res. 41 (2011) 923–931, https://doi.org/10.1016/j.cemconres.2011.05.006.
[45] S. Zhang, A. Keulen, K. Arbi, G. Ye, Waste glass as partial mineral precursor in alkali-activated slag/fly ash system, Cem. Concr. Res. 102 (2017) 29–40, https://doi.org/10.1016/j.cemconres.2017.08.012.
[46] C.A. Rees, J.L. Provis, G.C. Lukey, J.S.J. van Deventer, The mechanism of geopolymer gel formation investigated through seeded nucleation, Colloids Surfaces A Physicochem. Eng. Asp. 318 (2008) 97–105, https://doi.org/10.1016/j.colsurfa.2007.12.019.
[47] I. García Lodeiro, A. Fernández-Jimenez, A. Palomo, D.E. Macphee, Effect on fresh C-S-H gels of the simultaneous addition of alkali and aluminium, Cem. Concr. Res. 40 (2010) 27–32, https://doi.org/10.1016/j.cemconres.2009.08.004.
[48] Z. Li, M. Nedeljković, B. Chen, G. Ye, Mitigating the autogenous shrinkage of alkali-activated slag by metakaolin, Cem. Concr. Res. 122 (2019) 30–41, https://doi.org/10.1016/j.cemconres.2019.04.016.
[49] N.K. Lee, H.K. Lee, Reactivity and reaction products of alkali-activated, fly ash/slag paste, Constr. Build. Mater. 81 (2015) 303–312, https://doi.org/10.1016/j.conbuildmat.2015.02.022.
[50] D. Ravikumar, N. Neithalath, Reaction kinetics in sodium silicate powder and liquid activated slag binders evaluated using isothermal calorimetry, Thermochim. Acta 546 (2012) 32–43, https://doi.org/10.1016/j.tca.2012.07.010.
[51] Y. Ma, Microstructure and Engineering Properties of Alkali Activated Fly Ash -as an Environment Friendly Alternative to Portland Cement, (2013).
[52] Z. Yu, Microstructure Development and Transport Properties of Portland Cement-Fly Ash Binary Systems, (2015).
[53] J.L. Provis, P. Duxson, R.M. Harrex, J. van Deventer, Valorisation of Fly ashes by Geopolymerisation, Glob. NEST J. 11 (2009) 147–154.
[54] X. Gao, Q.L. Yu, H.J.H. Brouwers, Reaction kinetics, gel character and strength of ambient temperature cured alkali activated slag-fly ash blends, Constr. Build. Mater. 80 (2015) 105–115, https://doi.org/10.1016/j.conbuildmat.2015.01.065.
[55] D. Krizan, B. Zivanovic, Effects of dosage and modulus of water glass on early hydration of alkali-slag cements, Cem. Concr. Res. 32 (2002) 1181–1188, https://doi.org/10.1016/S0008-8846(01)00717-7.
[56] I. Ismail, S.A. Bernal, J.L. Provis, R. San Nicolas, S. Hamdan, J.S.J. Van Deventer, Modification of phase evolution in alkali-activated blast furnace slag by the incorporation of fly ash, Cem. Concr. Compos. 45 (2014) 125–135, https://doi.org/10.1016/j.cemconcomp.2013.09.006.
[57] M. Ben Haha, B. Lothenbach, G. Le Saout, F. Winnefeld, Influence of slag chemistry on the hydration of alkali-activated blast-furnace slag - part II: effect of Al2O3, Cem. Concr. Res. 42 (2012) 74–83, https://doi.org/10.1016/j.cemconres.2011.08.005.
[58] H. Dong, P. Gao, G. Ye, Characterization and comparison of capillary pore structures of digital cement pastes, Mater. Struct. Constr. (2017) 50, https://doi.org/10.1617/s11527-017-1023-9.
[59] Z. Zhang, L. Li, X. Ma, H. Wang, Compositional, microstructural and mechanical properties of ambient condition cured alkali-activated cement, Constr. Build. Mater. 113 (2016) 237–245, https://doi.org/10.1016/j.conbuildmat.2016.03.043.
[60] O.M. Jensen, P.F. Hansen, Autogenous deformation and RH-change in perspective, Cem. Concr. Res. 31 (2001) 1859–1865, https://doi.org/10.1016/S0008-8846(01)00501-4.
[61] P. Lura, Autogenous Deformation and Internal Curing of Concrete, Delft University of Technology, 2003.
[62] H. Le Chatelier, Sur les changements de volume qui accompagnent le durcissement des ciments, Bull. Soc. L'encouragement Pour L'industrie Natl. 5 (1900).
[63] O. Coussy, P. Dangla, T. Lassabatère, V. Baroghel-Bouny, The equivalent pore pressure and the swelling and shrinkage of cement-based materials, Mater. Struct. 37 (2004) 15–20.
[64] Y. Zuo, Experimental Study and Numerical Simulation of the Reaction Process and Microstructure Formation of Alkali-Activated Materials, Delft University of Technology, 2019.
[65] P. Lura, O.M. Jensen, K. Van Breugel, Autogenous shrinkage in high-performance cement paste: an evaluation of basic mechanisms, Cem. Concr. Res. 33 (2003) 223–232, https://doi.org/10.1016/S0008-8846(02)00890-6.
[66] T. Lu, Autogenous Shrinkage of Early Age Cement Paste and Mortar, Delft University of Technology, 2019.
[67] S. Nagataki, H. Gomi, Expansive admixtures (mainly ettringite), Cem. Concr. Compos. 20 (1998) 163–170.
[68] L.Y. Yang, Z.J. Jia, Y.M. Zhang, J.G. Dai, Effects of nano-TiO2on strength, shrinkage and microstructure of alkali activated slag pastes, Cem. Concr. Compos. 57 (2015) 1–7, https://doi.org/10.1016/j.cemconcomp.2014.11.009.
[69] M. Palacios, F. Puertas, Effect of shrinkage-reducing admixtures on the properties of alkali-activated slag mortars and pastes, Cem. Concr. Res. 37 (2007) 691–702.
[70] X. Gao, Q.L. Yu, H.J.H. Brouwers, Apply29Si,27Al MAS NMR and selective dissolution in identifying the reaction degree of alkali activated slag-fly ash composites, Ceram. Int. 43 (2017) 12408–12419, https://doi.org/10.1016/j.ceramint.2017.06.108.
[71] F. Puertas, M. Palacios, H. Manzano, J.S. Dolado, A. Rico, J. Rodríguez, A model for the CASH gel formed in alkali-activated slag cements, J. Eur. Ceram. Soc. 31 (2011) 2043–2056.
[72] J.N. Israelachvili, Intermolecular and Surface Forces, Academic press, 2011.
[73] X. Ouyang, D.A. Koleva, G. Ye, K. van Breugel, Understanding the adhesion mechanisms between C-S-H and fillers, Cem. Concr. Res. 100 (2017) 275–283, https://doi.org/10.1016/j.cemconres.2017.07.006.
[74] K.C. Marshall, R. STOUT, R. Mitchell, Mechanism of the initial events in the sorption of marine bacteria to surfaces, Microbiology 68 (1971) 337–348.
[75] M. Hermansson, The DLVO theory in microbial adhesion, Colloids Surfaces B Biointerfaces 14 (1999) 105–119.
[76] N. V Churaev, B. V Derjaguin, V.M. Muller, Surface Forces, Springer Science & Business Media, 2013.
[77] E.J.W. Verwey, J.T.G. Overbeek, J.T.G. Overbeek, Theory of the Stability of Lyophobic Colloids, Courier Corporation, 1999.
[78] X. Ouyang, Filler-Hydrates Adhesion Properties in Cement Paste System: Development of Sustainable Building Materials, (2017).
[79] A. Gmira, M. Zabat, R.-M. Pellenq, H. Van Damme, Microscopic physical basis of the poromechanical behavior of cement-based materials, Mater. Struct. 37 (2004) 3–14.
[80] G. Peschel, P. Belouschek, M.M. Müller, M.R. Müller, R. König, The interaction of solid surfaces in aqueous systems, Colloid Polym. Sci. 260 (1982) 444–451, https://doi.org/10.1007/BF01448150.
[81] J.N. Israelachvili, H. Wennerström, Entropic forces between amphiphilic surfaces in liquids, J. Phys. Chem. 96 (1992) 520–531, https://doi.org/10.1021/j100181a007.
[82] Y. Zuo, M. Nedeljković, G. Ye, Pore solution composition of alkali-activated slag/fly ash pastes, Cem. Concr. Res. 115 (2019) 230–250, https://doi.org/10.1016/j.cemconres.2018.10.010.
[83] J.A. Larbi, A.L.A. Fraay, J. Bijen, The chemistry of the pore fluid of silica fume-blended cement systems, Cem. Concr. Res. 20 (1990) 506–516.
[84] H.J.H. Brouwers, Others, alkali concentrations of pore solution in hydrating OPC, Cem. Concr. Res. 33 (2003) 191–196.
[85] Z. Li, M. Wyrzykowski, H. Dong, J. Granja, M. Azenha, P. Lura, G. Ye, Internal curing by superabsorbent polymers in alkali-activated slag, Cem. Concr. Res. (2020) (under review).
[86] C.J. Haecker, E.J. Garboczi, J.W. Bullard, R.B. Bohn, Z. Sun, S.P. Shah, T. Voigt, Modeling the linear elastic properties of Portland cement paste, Cem. Concr. Res. 35 (2005) 1948–1960, https://doi.org/10.1016/j.cemconres.2005.05.001.
[87] G. Ye, Experimental Study and Numerical Simulation of the Development of the Microstructure and Permeability of Cementitious Materials, (2003).
[88] A. Fernández-Jiménez, F. Puertas, et al., Effect of activator mix on the hydration and strength behaviour of alkali-activated slag cements, Adv. Cem. Res. 15 (2003) 129–136.
[89] Y. Ma, X. Yang, J. Hu, Z. Zhang, H. Wang, Accurate determination of the "time-zero" of autogenous shrinkage in alkali-activated fly ash/slag system, Compos. Part B Eng. (2019) 107367, https://doi.org/10.1016/J.COMPOSITESB.2019.107367.
[90] D.P. Bentz, E.J. Garboczi, D.A. Quenard, Modelling drying shrinkage in reconstructed porous materials: application to porous Vycor glass, Model. Simul. Mater. Sci. Eng. 6 (1998) 211.
[91] S. Prinsse, Alkali-Activated Concrete: Development of Material Properties (Strength and Stiffness) and Flexural Behaviour of Reinforced Beams over Time, Master Thesis (2017).
[92] L.F. Nielsen, A Research Note on Sorption, Pore Size Distribution, and Shrinkage of Porous Materials, Danmarks Tekniske Højskole. Laboratoriet for Bygningsmaterialer, 1991.
[93] K. Van Breugel, Relaxation of Young Concrete, (1980), p. 144.
[94] H. van der Ham, E. Koenders, K. van Breugel, Creep model uncertainties in early-age concrete simulations, Proc. Concreep. 8 (2008) 431–436.
[95] Z. Li, J. Liu, G. Ye, Drying shrinkage of alkali-activated slag and fly ash concrete; a comparative study with ordinary Portland cement concrete, Heron 64 (2019) 149.
[96] A. Kostiuchenko, Z. Li, G. Ye, Experimental study on creep behavior of alkali-activated concrete, Int. Conf. Innov. Mater. Sustain. Civ. Eng., Nanjing, 2019, p. 80.
[97] A. Boumiz, C. Vernet, F.C. Tenoudji, Mechanical properties of cement pastes and mortars at early ages: evolution with time and degree of hydration, Adv. Cem. Based Mater. 3 (1996) 94–106, https://doi.org/10.1016/S1065-7355(96)90042-5.
[98] Z. Li, S. Zhang, X. Liang, G. Ye, Cracking potential of alkali-activated slag and fly ash concrete subjected to restrained autogenous shrinkage, Cem. Concr. Compos. (2020) (under review).
[99] P. Lura, M. Wyrzykowski, Influence of aggregate restraint on volume changes: Experiments and Modelling, Concreep, 2015, pp. 17–23 , https://doi.org/10.1061/9780784479346.
[100] D.W. Hobbs, Influence of aggregate restraint on the shrinkage of concrete, ACI J. Proc. 71 (1974) 445–450, https://doi.org/10.14359/7089.